

# Sub-Nyquist computational ghost imaging with orthonormalized colored noise pattern

Xiaoyu Nie,<sup>1,2</sup> Xingchen Zhao,<sup>1</sup> Tao Peng,<sup>1,\*</sup> and Marlan O. Scully<sup>1,3</sup>

<sup>1</sup>*Department of Physics and Astronomy, Texas A&M University, College Station, Texas, 77843, USA*

<sup>2</sup>*Physics Department, Xi'an Jiaotong University, Xi'an, Shaanxi 710049, China*

<sup>3</sup>*Baylor Research and Innovation Collaborative, Baylor University, Waco, 76706, USA*

(Dated: June 12, 2022)

Computational ghost imaging generally requires a large number of pattern illumination to obtain a high-quality image. The colored noise speckle pattern was recently proposed to substitute the white noise pattern in a variety of noisy environments and gave a significant signal-to-noise ratio enhancement even with a limited number of patterns. We propose and experimentally demonstrate here an orthonormalization approach based on the colored noise patterns to achieve sub-Nyquist computational ghost imaging. We tested the reconstructed image in quality indicators such as the contrast-to-noise ratio, the mean square error, the peak signal to noise ratio, and the correlation coefficient. The results suggest that our method can provide high-quality images while using a sampling ratio an order lower than the conventional methods.

Computational ghost imaging (CGI) [1–3], an ameliorated scheme on traditional ghost imaging (GI) [4–7], owns the ability to reconstruct the object via single bucket detector. CGI also grants advantages in an expanding range of non-conventional applications such as wide spectrum imaging [8, 9] and depth mapping [10, 11]. It also finds application to various fields, such as temporal imaging [3], X-ray imaging [12], remote sensing [13], *etc.*. However, its sampling number is usually comparable to the total number of pixels in the speckle pattern to keep good imaging quality, thus is time consuming and resource intensive. In addition, it is only suitable for static object reconstruction.

Various methods have been proposed to overcome this problem [14–19]. One typical and effective way is the orthonormalization method [18]. This method introduces a data post-processing algorithm to improve the reconstructing process in a GI system with pseudo-thermal light. By applying the Gram-Schmidt process on the noise patterns and intensity sequence collected by the bucket detector, the required sampling number is reduced. However, such a method is sensitive to noise and the image quality is not even comparable with standard CGI when the pattern number is large enough. Traditionally, Gaussian white noise speckle pattern is used for GI. The spatial distribution of the light field amplitude is Gaussian, and the phase associated with the field amplitude is random. Recently, we developed a method to generate the so-called colored noise speckle pattern for CGI by customizing the power spectrum density of the speckle patterns [20]. Unlike white noise, colored noise generally has non-zero cross-correlation between neighborhood pixels. Sub-Rayleigh imaging was demonstrated with the blue noise pattern which has negative cross-correlation between two adjacent pixels. The pink noise pattern allowed us to image in a variety of noisy environments.

In this letter, we introduce a novel method on the combination of the colored noise and Orthonormalization methods together to substantially reduce the number of sampling and overcome the drawback of pink noise patterns. We also compare the orthonormalization colored noise GI (OCGI) with orthonormalization white noise GI (OWGI), traditional white noise GI (WGI), and pink noise GI (PGI). The results are tested using the quality indicators such as the Contrast-to-Noise Ratio (CNR), the Peak Signal to Noise Ratio (PSNR), the Correlation Coefficient (CC), and the Mean Square Error (MSE). We show that OCGI always has the best performance. It can reduce the sample rate one order lower while still obtain the same image quality as that of standard CGI. It is also robust to noise interference.

The experimental setup is shown in Fig. 1. This is a typical CGI setup, a CW laser is used to illuminate the digital micromirror device (DMD), where the speckle patterns with designed distributions are loaded. The pattern generated by the DMD is then imaged onto the object with letters 'OH' etched on an opaque plate. A bucket detector is put right after the object to record the transmitted light intensity. The DMD contains tiny pixel-mirrors each measuring  $16\ \mu\text{m} \times 16\ \mu\text{m}$ . In the experiment, each noise patterns has  $54 \times 98$  independent pixels, each independent pixel consists of  $10 \times 10$  mirrors.

Firstly, the Gaussian white and pink noise patterns are generated by applying inverse Fourier transformation upon the spectrum in which the spatial frequencies are defined as  $\omega^0$  and  $\omega^{-1}$  [20]. Random phase matrices are also assigned to each pattern. The Gram-Schmidt process is then performed to orthonormalize the patterns. We note here that, after the orthonormalization, the spatial frequency of the pink noise pattern is gradually changed to blue noise distribution, as shown in Fig. 2. In other words, the spatial frequency of the orthonormalized pattern covers a broad spectrum range from pink to blue, which is why we named it colored noise pattern. The initial colored patterns are

---

\*Electronic address: taopeng@tamu.edu

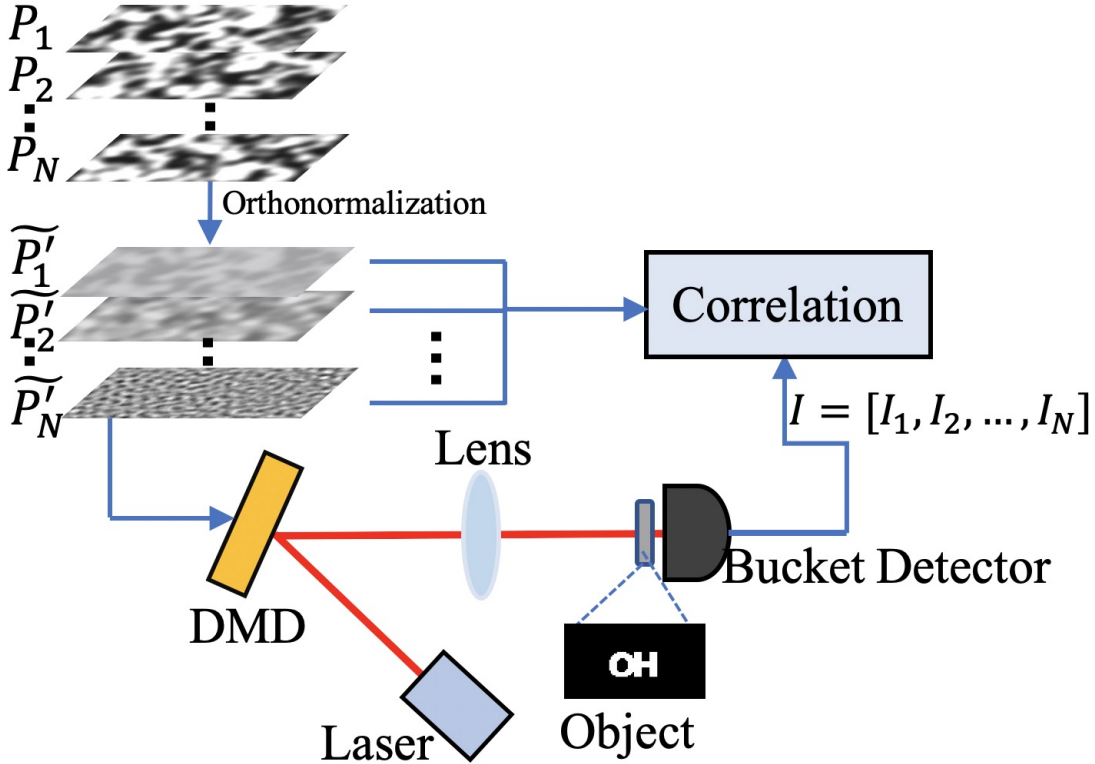


FIG. 1: Schematic of the setup. The digital micromirror device (DMD) is illuminated by a CW laser. Orthonormalized patterns are loaded on the DMD then imaged onto the object plane. Correlation measurement is made between the pattern and the intensity measured from the bucket detector.

matrices  $P_1, P_2, P_3, \dots, P_N$ , and the orthonormalized patterns are matrices  $\widetilde{P}_1, \widetilde{P}_2, \widetilde{P}_3, \dots, \widetilde{P}_N$ , all of which contain  $54 \times 98$  elements. We define the projection coefficient  $c_{mn}$  by

$$c_{mn} = \frac{P_m \cdot \widetilde{P}_n}{\widetilde{P}_n \cdot \widetilde{P}_n} \quad (1)$$

And the orthonormalized patterns can be generated by

$$\widetilde{P}_1 = P_1 \quad (2)$$

$$\widetilde{P}_m = P_m - \sum_{n=1}^{m-1} c_{mn} \widetilde{P}_n \quad (3)$$

Then, we re-normalize the histogram of  $\widetilde{P}_1, \widetilde{P}_2, \widetilde{P}_3, \dots, \widetilde{P}_N$  to  $[0, 255]$ , which we define as  $\widetilde{P}'_1, \widetilde{P}'_2, \widetilde{P}'_3, \dots, \widetilde{P}'_N$ . According to the number of orthogonal vector space, we generate 5292 patterns for each kind, which is equal to the number of total pixel in single pattern. We note here that, unlike the post-processing method shown in [18], we directly generate these orthonormalized patterns and apply them to DMD. Therefore, the orthonormalization coefficients and patterns are done at one time. In addition, we don't have any intensity loses during the orthonormalization process. In our scheme, the intensity is measured as

$$I_i = T \cdot \widetilde{P}'_i, \quad (4)$$

where  $T$  is the transmission coefficient of the object,  $\widetilde{P}'_i$  is the  $i$ -th orthonormalized pattern. As shown in Fig. 1, the image is retrieved by calculating the correlation between patterns and collected light intensity sequence as

$$g^{(2)} = \frac{1}{N} \sum_{i=1}^N \widetilde{P}'_i I_i - \frac{1}{N^2} \sum_{i=1}^N \widetilde{P}'_i \times \sum_{i=1}^N I_i, \quad (5)$$

where  $N$  is the sampling number. We define  $\beta$  as the ratio between the sampling number  $N$  and the number of speckle in each pattern  $N_{pixel}$  as

$$\beta = \frac{N}{N_{pixel}} \quad (6)$$

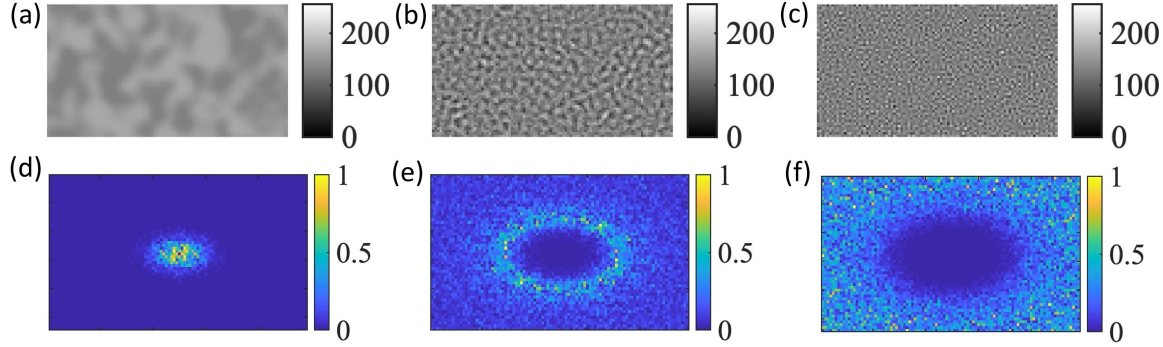


FIG. 2: The orthonormalized colored noise pattern: (a) the 1st pattern, (b) the 1000th pattern, (c) the last pattern (5292th); (d), (e), and (f) are normalized spatial frequency distribution of the 1st pattern, the 1000th pattern, and the 5292th pattern, respectively.

Now, we explore the properties of the orthonormalized pattern by analyzing its spatial frequency, its auto- and cross-correlation. To begin with, the spatial frequencies are shown in Fig. 2. We see that when the pattern number increases, the frequency peak is moving to the higher end. This suggests that the pattern is gradually changing for pink noise distribution to blue noise distribution under the orthonormalization process. This is easy to understand since the orthonormalization protocol naturally requires that the patterns to be orthogonal including the spatial frequency domain. So the OCGI maintains the pink noise's advantage when the sampling number is small, and it can continuously enhance the resolution when increasing the number of sampling. Indeed, the OCGI owns the OWGI's feature when the sampling number close to the number of total pixel in one pattern, as shown in Fig. 3.

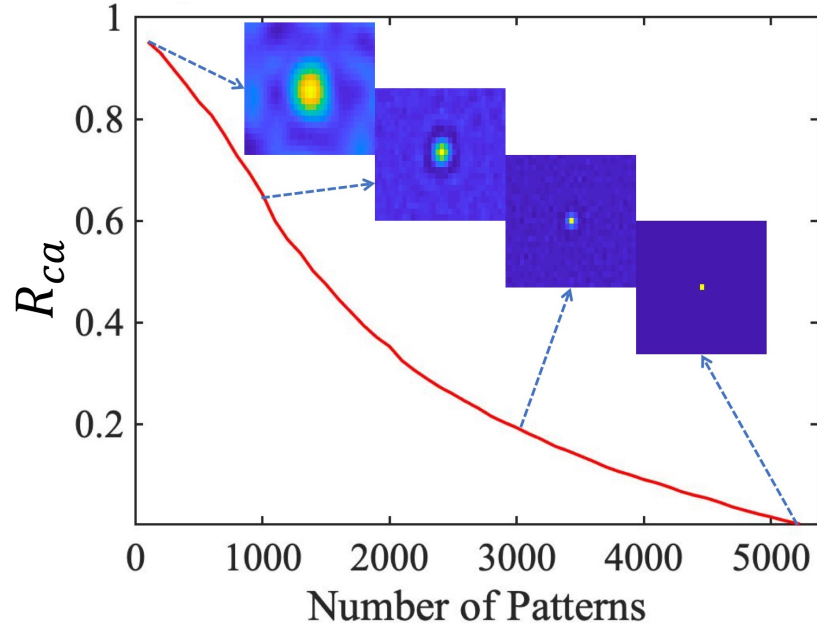


FIG. 3: Cross-auto correlation ratio as a function of pattern number. Inserted pictures: from top left to bottom right, 2D auto- and cross-correlation of total pattern number 100, 1000, 3000, and 5292.

A random pixel  $p(x, y)$  is chosen and its auto-correlation and cross correlation with all other pixels are calculated.

The cross-auto correlation ratio  $R_{ca}$  is defined as,

$$R_{ca} = \frac{g_{p(x-1,y)}^{(2)} + g_{p(x+1,y)}^{(2)} + g_{p(x,y-1)}^{(2)} + g_{p(x,y+1)}^{(2)}}{4g_{p(x,y)}^{(2)}} \quad (7)$$

The relationships are shown in Fig. 3. From the pink line we can see that the ratio is gradually dwindling, the cross correlation starts from 1 when  $\beta$  is small and eventually decreases to 0 when  $\beta = 1$ , which is the same as the white noise pattern. In a word, from the arbitrary unit pattern's spatial frequency distribution, we can precisely predict the change of results during the image retrieving process with the OCGI method. It is also expected that the OCGI and OWGI measurements will converge to the same results when  $\beta$  approaches 1, as shown in the following.

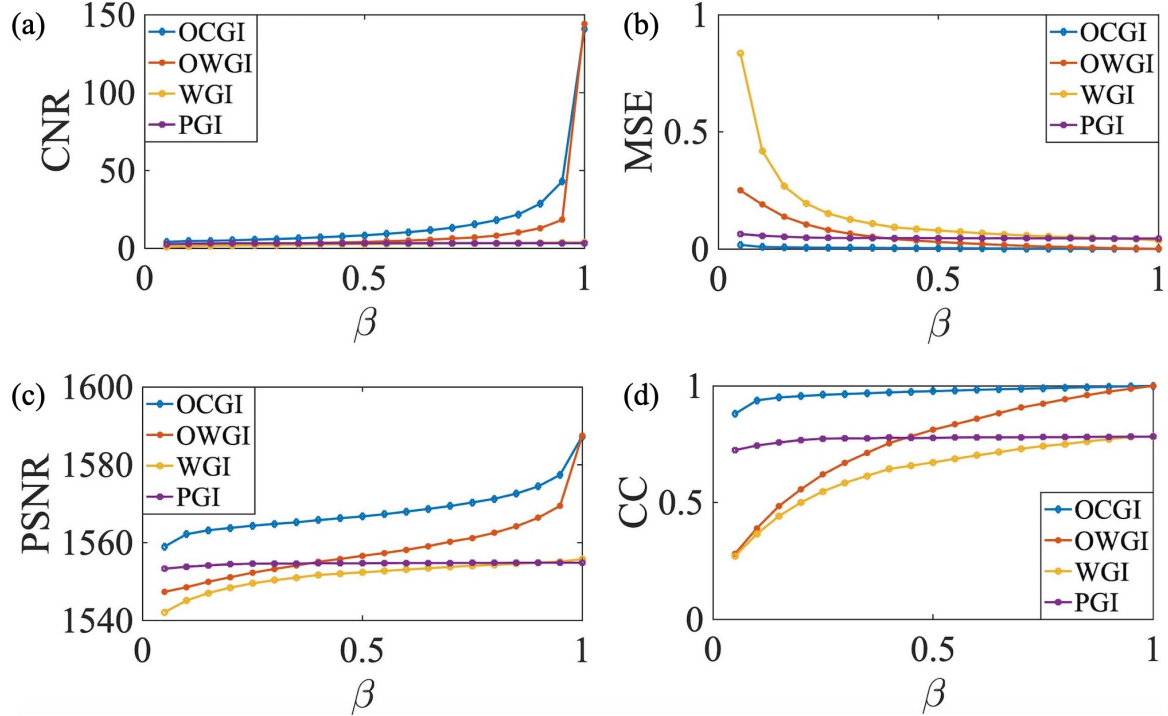


FIG. 4: Simulation with no noise. Image qualities via different frame numbers by CGI in ideal condition. (a) CNR, (b) MSE, (c) PSNR, and (d) CC.

To test the feasibility of the OCGI method, we run a simulation firstly in ideal condition without environmental and system noise. To better judge the performance of various methods, *i.e.*, the OCGI, OWGI, WGI, and PGI, we utilize four evaluating indicators of image quality, *i.e.*, CNR, MSE, PSNR, and CC [18, 21–23]:

$$CNR = \frac{\langle G_{(o)} \rangle - \langle G_{(b)} \rangle}{\sqrt{Var[G_{(o)}] + Var[G_{(b)}]}} \quad (8)$$

$$MSE = \frac{1}{N_{pixel}} \sum_{i=1}^{N_{pixel}} \left[ \frac{G_i - X_i}{\langle G_{(o)} \rangle} \right]^2 \quad (9)$$

$$PSNR = 10 \times \log_{10} \left[ \frac{(2^k - 1)^2}{MSE} \right] \quad (10)$$

$$CC = \frac{Cov(G, X)}{\sqrt{Var(G)Var(X)}} \quad (11)$$

Here,  $X$  is the reference matrix calculated by

$$X_i = \begin{cases} \langle G_{(o)} \rangle & , \text{Transmission} = 1 \\ \langle G_{(b)} \rangle & , \text{Transmission} = 0 \end{cases} \quad (12)$$

$G_{(o)}$  represents pixels in the correlation results that the light ought to be transmitted, *i.e.*, the object area, while  $G_{(b)}$  represents pixels in the correlation results that the light ought to be blocked, *i.e.*, the background area.  $k$  is the gray level of the image, and in our experiment  $k \equiv 8$ .

As shown in Fig. 4, the OCGI, similar to the PGI, gives a stronger signal in the low sample rate domain, as demonstrated in our previous study[20]. The OCGI has always the best image quality. It is only when the image quality is saturated as the pattern number reaches maximum, the OWGI and OCGI have almost the same behavior. Both of them are still much better than the WGI and PGI. Here the orthonormalization process completely smears the weakness of PGI whose image quality is almost smooth from the beginning to the end, and strengthens the PGI's advantage at the small level of sampling.

The advantage of OCGI is further demonstrated when we introduce background noise into the system, since in real experimental condition the noises such as background noise, the quantization error, diffraction and thermal noise of detectors are more or less unavoidable. We run another simulation with noise level at  $\pm 1\%$  signal. The values of evaluating indicators are presented in Fig. 5, from which we can see that MSE is about the same as the noise-free case. OCGI still maintains the best in these imaging methods. CNR is dramatically decreased for all methods, when  $\beta$  is large. Nevertheless, it should be noted that there are peaks clearly shown in the Fig. 5(c) and Fig. 5(d). The PSNR and CC of OCGI reach their highest value when  $\beta \sim 0.1$ , then slowly decrease and finally reach the same value as that of the OWGI. It suggests that during the orthonormalization process of the colored noise pattern, there exists an optimum sampling rate for the noise-free feature. Again, the orthonormalized results are always better than the conventional patterns.

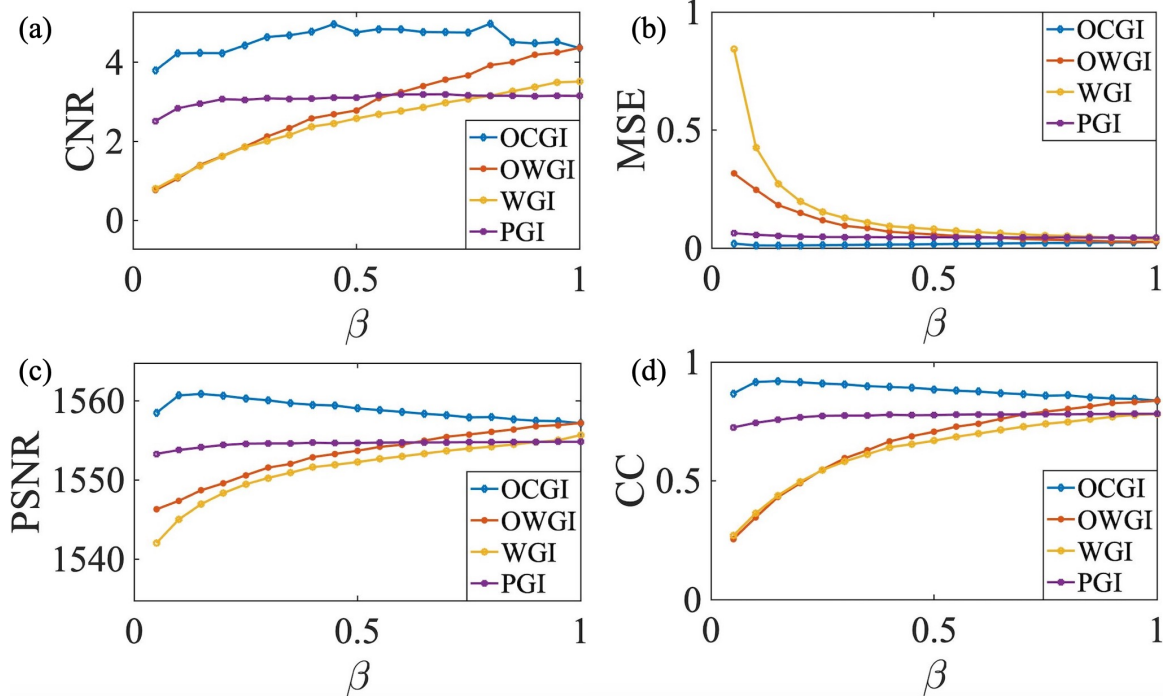


FIG. 5: Simulation with added noise. Image qualities via different frame numbers by CGI with noise at  $\pm 1\%$  signal level. (a) CNR, (b) MSE, (c) PSNR, and (d) CC.

In the experiment, we perform measurement on the object 'OH'. The main results are shown in Fig. 6(a). The  $N_{pattern}$  represents the patterns we apply on the DMD to retrieve the image, while the  $N_{pixel}$  symbolizes the total pixel contained in each pattern. As mentioned earlier,  $N_{pixel} = 54 \times 98$  in our experiment. From Fig. 6 we see that when  $\beta$  is only 0.05, the OCGI already gives an image while all the other methods show no image at all. OCGI, OWGI and WGI all give a clear image at  $\beta \sim 0.5$ , but the image obtained with OCGI is clearer than that of OWGI, and both of them are better than WGI. On the other hand, PGI failed to give a clear image even when  $\beta = 1$ . This

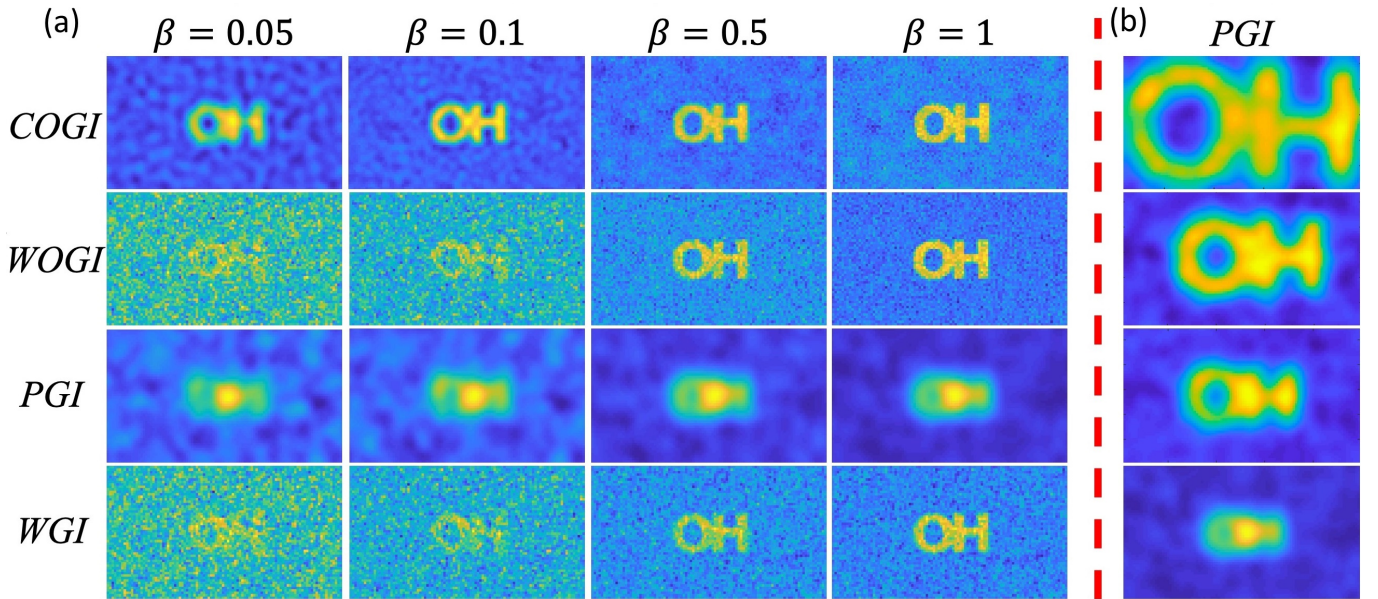


FIG. 6: Experimental results. (a) Different types of noise pattern with various  $\beta$ . (b) PGI with different object size at  $\beta = 1$ . the size of the letters, from top to bottom, are: 4, 3, 2, and 1 times of that used for (a).

is due to the relatively small object size compared with the pixel size. To verify that, we then gradually enlarge the object size 2, 3, and 4 times for PGI, as shown in Fig. 6(b). We see that when the object size is large enough, the PGI gives a clear image. We conclude that the quality of image in OCGI is better than other conventional methods, particularly when  $\beta = 0.1$  where we get the optimum results from the simulation with noise as well. The PGI method, on the other hand, is limited to the object size and cannot be used for the resolution-limit imaging. To

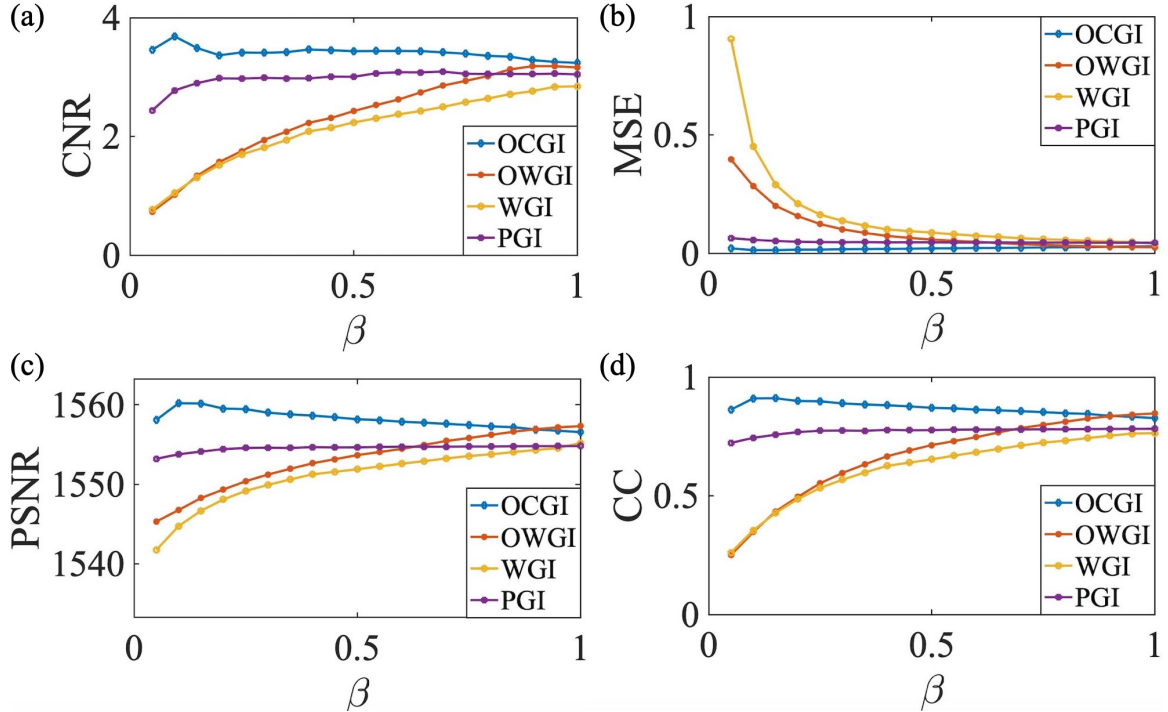


FIG. 7: Image qualities via different frame numbers in the experiment. (a) CNR, (b) MSE, (c) PSNR, and (d) CC.

further compare the results, we utilize those four evaluating indicators of image quality again. The results are shown in Fig. 7.

We can see that the experimental results and the simulation results almost exactly match. Nevertheless, as shown in Fig. 6, even though the quality of images retrieved from OCGI are the best when  $\beta = 0.1$  if judged by evaluating indicator, the results when  $\beta = 1$  seem to have stronger visibility. It is because they have sharper edge compared to results when  $\beta = 0.1$ . The reason is when  $\beta = 1$  the cross-correlation disappears, thus no contribution to the area where the object is opaque. So when  $\beta = 0.1$  the results have substantially strong SNR, when  $\beta = 1$  the measurements restore the image authentically. Those parameters also give us some indication of the optimal frame rate to choose depending on different experimental goal.

In conclusion, we have developed a method based on the orthonormalized colored noise pattern in the CGI system to yield image reconstruction results with high quality when the sampling number is small, and with continuously improvement during the further sampling, which is the weakness of the traditional pink noise pattern. The major advantage of this scheme is that it makes use of the continuously changing cross-correlation from the orthonormalized colored noise patterns to overcome the difficulties faced by conventional white and pink noise. Meanwhile, this method is easy to implement because of its simple setup and rapid image reconstruction; this method is also immune to noise.

#### Funding.

Air Force Office of Scientific Research (Award No. FA9550-20-1-0366 DEF), Office of Naval Research (Award No. N00014-20-1-2184), Robert A. Welch Foundation (Grant No. A-1261), National Science Foundation (Grant No. PHY-2013771).

#### Disclosures.

The authors declare no conflicts of interest.

---

[1] J. H. Shapiro, *Physical Review A* **78**, 061802 (2008).

[2] Y. Bromberg, O. Katz, and Y. Silberberg, *Physical Review A* **79**, 053840 (2009).

[3] F. Devaux, P.-A. Moreau, S. Denis, and E. Lantz, *Optica* **3**, 698 (2016).

[4] T. B. Pittman, Y. H. Shih, D. V. Strekalov, and A. V. Sergienko, *Physical Review A* **52**, R3429 (1995).

[5] R. S. Bennink, S. J. Bentley, R. W. Boyd, and J. C. Howell, *Physical review letters* **92**, 033601 (2004).

[6] A. Valencia, G. Scarcelli, M. D'Angelo, and Y. Shih, *Physical review letters* **94**, 063601 (2005).

[7] D. Zhang, Y.-H. Zhai, L.-A. Wu, and X.-H. Chen, *Optics letters* **30**, 2354 (2005).

[8] M. P. Edgar, G. M. Gibson, R. W. Bowman, B. Sun, N. Radwell, K. J. Mitchell, S. S. Welsh, and M. J. Padgett, *Scientific reports* **5**, 10669 (2015).

[9] N. Radwell, K. J. Mitchell, G. M. Gibson, M. P. Edgar, R. Bowman, and M. J. Padgett, *Optica* **1**, 285 (2014).

[10] G. A. Howland, D. J. Lum, M. R. Ware, and J. C. Howell, *Optics express* **21**, 23822 (2013).

[11] M.-J. Sun, M. P. Edgar, G. M. Gibson, B. Sun, N. Radwell, R. Lamb, and M. J. Padgett, *Nature communications* **7**, 1 (2016).

[12] Y. Klein, A. Schori, I. Dolbnya, K. Sawhney, and S. Shwartz, *Optics express* **27**, 3284 (2019).

[13] B. I. Erkmen, *JOSA A* **29**, 782 (2012).

[14] V. Katkovnik and J. Astola, *JOSA A* **29**, 1556 (2012).

[15] M. Aßmann and M. Bayer, *Scientific reports* **3**, 1 (2013).

[16] M.-J. Sun, L.-T. Meng, M. P. Edgar, M. J. Padgett, and N. Radwell, *Scientific reports* **7**, 1 (2017).

[17] M. Lyu, W. Wang, H. Wang, H. Wang, G. Li, N. Chen, and G. Situ, *Scientific reports* **7**, 1 (2017).

[18] B. Luo, P. Yin, L. Yin, G. Wu, and H. Guo, *Optics express* **26**, 23093 (2018).

[19] F. Wang, H. Wang, H. Wang, G. Li, and G. Situ, *Optics express* **27**, 25560 (2019).

[20] X. Nie, F. Yang, X. Liu, X. Zhao, R. Nessler, Z. Li, T. Peng, M. S. Zubairy, and M. O. Scully, *arXiv preprint arXiv:2009.14390* (2020).

[21] P. Zerom, Z. Shi, M. N. O'Sullivan, K. W. C. Chan, M. Krogstad, J. H. Shapiro, and R. W. Boyd, *Physical Review A* **86**, 063817 (2012).

[22] X. Xu, E. Li, X. Shen, and S. Han, *Chinese Optics Letters* **13**, 071101 (2015).

[23] J. Li, D. Yang, B. Luo, G. Wu, L. Yin, and H. Guo, *Optics Letters* **42**, 1640 (2017).

[24] R. E. Meyers, K. S. Deacon, and Y. Shih, *Applied Physics Letters* **98**, 111115 (2011).